**Citation for published item:**

Cooper, George F. and Macpherson, Colin G. and Blundy, Jon D. and Maunder, Benjamin and Allen, Robert W. and Goes, Saskia and Collier, Jenny S. and Bie, Lidong and Harmon, Nicholas and Hicks, Stephen P. and Iveson, Alexander A. and Prytulak, Julie and Rietbrock, Andreas and Rychert, Catherine A. and Davidson, Jon P. and The VoiLA Team, (2020) 'Variable water input controls evolution of the Lesser Antilles volcanic arc.', Nature., 582 . pp. 525-529.

**Further information on publisher's website:**

https://doi.org/10.1038/s41586-020-2407-5

# Variable water input controls evolution of the Lesser Antilles volcanic arc

George F. Cooper[1*], Colin G. Macpherson[2], Jon D. Blundy[1], Benjamin Maunder[3], Robert W. Allen[3], Saskia Goes[3], Jenny Collier[3], Lidong Bie[5], Nick Harmon[4], Stephen P. Hicks[3], Alexander A. Iveson[2], Julie Prytulak[2], Andreas Rietbrock[5,6], Catherine Rychert[4], Jon P. Davidson[2] and the VoiLA team

[1] School of Earth Sciences, University of Bristol, Wills Memorial Building, Bristol BS8 1RJ, UK

[2] Department of Earth Sciences, Durham University, Science Labs, Durham DH1 3LE, UK

[3] Department of Earth Science and Engineering, Imperial College London, SW7 2AZ, UK

[4] University of Southampton, National Oceanography Centre, European Way, Southampton, SO14 3ZH, UK

[5] Department of Earth Ocean & Ecological Sciences, University of Liverpool, UK

[6] Geophysical Institute (GPI), Karlsruhe Institute of Technology, 76187 Karlsruhe, Germany

*corresponding author, email: CooperG3@cardiff.ac.uk, current address: School of Earth and Ocean Sciences, Cardiff University, Cardiff, CF10 3AT, UK

A list of authors and their affiliations appears at the end of the paper

**Oceanic lithosphere carries volatiles, notably water, into the mantle via subduction at convergent plate boundaries. This subducted water exercises a key control on the production of magma, earthquakes, formation of continental crust and mineral resources. However, identifying different potential fluid sources (sediments, crust and**

**mantle lithosphere) and tracing fluids from their release to observed surface expressions has proved challenging[1]. The two Atlantic subduction zones are valuable end members to study this deep water cycle because hydration in Atlantic lithosphere, produced by slow spreading, is expected to be highly non-uniform[2]. As part of an integrated, multi-disciplinary project in the Lesser Antilles[3], we studied boron trace element and isotopic fingerprints of melt inclusions. These reveal that serpentine, i.e. hydrated mantle rather than crust or sediments, is a dominant supply of subducted water to the central arc. This serpentine is most likely to reside in a set of major fracture zones subducted beneath the central arc over the past ~10 Myr. Dehydration of these fracture zones is consistent with the locations of the highest rates of earthquakes and prominent low shear velocities, as well as time-integrated signals of higher volcanic productivity and thicker arc crust. These combined geochemical and geophysical data provide the clearest indication to date that the structure and hydration of the downgoing plate are directly connected to the evolution of the arc and its associated hazards.**

The 750 km-long Lesser Antilles volcanic arc (LAA), located along the eastern margin of the Caribbean Plate, is the result of slow (1-2 cm/year) westward subduction of Atlantic and proto-Caribbean oceanic lithosphere (Fig 1). Water hosted in hydrous phases within the subducting plate will be released as the slab sinks into the mantle and warms up. As the water migrates out of the slab the stress on faults is reduced, causing earthquakes. At the same time, the addition of water to the overlying mantle wedge reduces the solidus temperature which may enhance melting. LAA magma production rates lie at the lower end of the global range, probably due to the low convergence rates, and are very unevenly distributed, being greatest in the centre of the arc (Dominica and Guadeloupe)[4]. The LAA also displays notable along-arc variations in geochemistry, volcanic activity, crustal structure, and seismicity[5–8]. Subducting plate velocity and age are often held responsible for variations in convergent margin behaviour[9] but are unlikely to have first-order influence on lateral variations within the LAA as neither vary significantly along-strike. Instead, variations in LAA magmatism and seismicity have been proposed to reflect; (i) a combination of a strong north to south increase in sediment input[10], (ii) subduction of bathymetric ridges below the central arc[11], which may enhance plate stress and coupling, (iii) and/or subduction of strongly hydrated fracture zones[12] at several locations along arc (Fig. 1).

Current plate reconstructions[13] show the northern LAA to be underlain by ~90 Ma subducted lithosphere that formed at the Equatorial Mid-Atlantic Ridge and includes the Marathon and Mercurius fracture zones (Fig. 1), whereas beneath the southern LAA, the subducted lithosphere is up to 120 Ma old and formed at the, now-fully subducted, proto-Caribbean mid-ocean ridge. The seafloor spreading rates were slow in both cases. The boundary between the two seafloor-spreading domains is clearly visible in both bathymetric and gravity data, projecting from the Demerera Plateau toward the central islands before becoming obscured by the accretionary prism around Barbados (Fig. 1; Extended Data Fig. 1).

Hydration of lithosphere formed by intermediate or fast spreading occurs mainly in the mafic crust through faults that form as the plate bends into the trench. By contrast, slow spreading produces highly tectonised oceanic lithosphere with relatively thin mafic crust, pronounced faults, and sections of upper mantle material exposed at the seafloor[14]. The transform faults at slow spreading ridges, which manifest as fracture zones in mature oceanic crust, are more seismically active and penetrate to greater depths than in faster-spread lithosphere[15]. These large-scale faults provide pathways for seawater and low/medium temperature alteration including hydration of the mantle mineral olivine to serpentine[16]. Serpentine, in the form of antigorite, can hold up to 13 wt. % structural water, at least double the water capacity of hydrated mafic crust. Thus, subduction of serpentinized mantle lithosphere has the potential to supply substantial volumes of fluid to magmatic arcs. In order to evaluate along-arc variations of slab-derived fluid sources (e.g. sediment, oceanic crust, or serpentinized mantle lithosphere), we measured trace element concentrations and boron isotopic ratios of melt inclusions along the entire LAA. To investigate how fluids influence arc magma genesis and evolution we compare these geochemical proxies for slab-derived fluids with newly-acquired geophysical data[3], and with the predicted positions of subducted fracture zones and the proto-Caribbean/Equatorial Atlantic plate boundary below the arc at different times.

In subduction zone magmas, boron and its isotopes trace contributions from fluids released by the subducting plate[17,18]. Boron is fluid mobile, and a high ratio of boron to fluid-immobile elements, like Ti, Nb, or Zr, in arc magmas suggests boron is principally supplied by subducting-plate fluids[19]. Serpentine-derived boron is enriched in $^{11}B$ compared to $^{10}B$, producing distinctively elevated $\delta^{11}B$ values of +7‰ to +20‰[17] ($\delta^{11}B = ((^{11}B/^{10}B)_{sample}/(^{11}B/^{10}B)_{standard} - 1) \times 10^3$). As a result, arc magmas produced through mantle melting induced by serpentine-derived fluids have significantly higher $\delta^{11}B$ values (up to +18‰[20]) than MORB-source mantle (-7.1 ± 0.9‰[21]). Fluids derived from subducted sediments have yet a different distinct chemical signature[22]. Sediments in ocean drill cores east of the LAA contain terrigenous turbidites, pelagic clays, and ashy siliceous clays[23]. Although these sediments are enriched in boron (50-160 ppm B), they have significantly lower $\delta^{11}B$ values (approximately -15 to +5‰[21]) than serpentine-derived fluids at sub-arc depths[24].

Using secondary ion mass spectrometry (SIMS), we measured 198 glassy, clinopyroxene-hosted melt inclusions for volatiles ($H_2O$, $CO_2$) and trace elements, of which 92 were further analysed for boron isotopic composition. The analysed melt inclusions are from fresh volcanic deposits assumed to be <<1 million years old (Ma), and range from low-MgO, high-alumina basalt (MgO = 1.8-3.5 wt. %, $Al_2O_3$ = 15.3-19.1 wt. %) to rhyolite (≤78 wt. % $SiO_2$; Fig. 2). All of these compositions have undergone some level of magmatic differentiation in the shallow crust, thus none can be considered primary, however, the boron isotopic signature is largely determined by the source rather than subsequent differentiation processes[25,26]. We supplemented our dataset with all previously published LAA melt inclusion analyses (*n*>1000) available from the GEOROC database.

LAA melt inclusions are characterised by dissolved water contents of up to 9.1 wt. % $H_2O$, with a large range for individual islands (Fig. 2). However, water contents of melt inclusions are affected by differentiation processes during crustal storage and thus are a poor proxy for primary magmatic water contents. Water content will increase in a melt undergoing undersaturated crystallisation, remain constant under water saturated conditions, and be lost from melt during late-stage degassing. Further modification of water in melt inclusions can occur due to post entrapment crystallisation and/or diffusive water loss. Ratios of fluid mobile to fluid immobile trace elements, such as B/Nb (Fig. 2), are more reliable indicators of the contribution of fluids, as both elements behave similarly during melting and magmatic differentiation. Our data shows high ratios of B/Nb in the central arc which most probably reflect a particularly fluid and B-rich magmatic source.

The new $\delta^{11}B$ values for LAA melt inclusions vary from -2.8‰ to +11.2‰ (Fig. 2), which spans much of the global arc range (-9‰ to +16‰[17]). Melt inclusions with the highest $\delta^{11}B$ values are from the central arc (islands of Guadeloupe and Dominica; Fig. 2). $\delta^{11}B$ variation within each volcanic centre is unlikely to be due to crustal differentiation because there are no systematic trends in $\delta^{11}$B with indicators of differentiation (e.g. $SiO_2$ and Rb/Sr, Extended Data Fig. 3). This is consistent with prior findings that fractional crystallisation has negligible effect on melt $\delta^{11}$B values[25,26]. Crustal assimilation during open-system differentiation may also modify $\delta^{11}$B and B/Nb, but inputs from this source likely have a similar isotopic and geochemical composition to AOC and sediment[22]. Assimilation of LAA crust would lower melt $\delta^{11}$B values during differentiation, a trend that is not observed in our data (Extended Data Fig. 3). Although there is a range of melt inclusion $\delta^{11}$B values within each single volcanic centre (e.g 3.5 ‰ in Martinique) there are clear $\delta^{11}$B differences between neighboring volcanic centres with similar major element chemistry. Therefore, we interpret the distinct $\delta^{11}$B values in evolved melt inclusions at each island as a reflection of differences between the mantle source regions of each island, such that boron isotopes provide a robust tracer for the fluid source[18].

We interpret the $\delta^{11}$B differences between islands and the systematic $\delta^{11}$B change along the arc to result from variable involvement of fluids from two distinct sources: (1) altered oceanic crust (AOC) and sediment; and (2) serpentine dehydration (Fig. 3). In the central portion of the arc, melt inclusions from Guadeloupe and Dominica have $\delta^{11}$B values significantly greater than +5‰. Of the available sources, only fluid with > 60% contribution from serpentine dehydration has the capacity to generate this isotopic signature (Fig. 3). The lower $\delta^{11}$B values found in the north and south of the arc can be attributed primarily to fluid released by dehydration of AOC and sediment (Fig. 3). However, there is no simple relationship between $\delta^{11}$B and indicators of varying volume of fluid addition (e.g. B/Be and B/Nb; Extended Data Fig. 3). In contrast to Guadeloupe and Dominica, St. Lucia melt inclusions from this study have a high net fluid contribution based on the Nb/B values, but we estimate <30% of this originates from serpentine. Therefore, the total volume of fluid is decoupled from the proportion of different sources from which each fluid is derived. In the north and south of the arc, with the exception of St. Vincent, the proportion of fluid derived from serpentine is lower than in the central arc. Based on boron isotopes it is not possible to distinguish if the serpentinite fluids are derived from the slab or from recycled forearc material[20,27]. However, a peak in seismicity occurs in the central arc at the depths where models predict dehydration of peridotite in the slab (120-160km)[9,28]. In conjunction with the abundance of serpentinised peridotite expected in slow-spread lithosphere[14,29] this provides an argument for slab-hosted serpentine being the main deliverer of fluid to LAA mantle wedge.

We compared our geochemical results to a range of independent observations that may be expressions of fluid release (Fig 4). As these observations sample different parts of the subduction system in space and time, we modelled expected excess hydration i.e., fluid derived from fractures zones, to the arc over the past 25 Myr (Fig. 4b), assuming that the known fracture zones and plate boundary between the proto-Caribbean and Atlantic bring extra water in the form of serpentine (see Methods).

If higher recent fluid fluxes below the arc were to cause an increase in magmas production then we might expect to see boron isotope ratios (Fig 4a) and/or intraslab seismicity rates[30] correlate with volcanic production rates[4] (Fig. 4 e and f). Slab seismicity is often attributed to dehydration embrittlement[31], and the depths to which seismicity extends[30] is consistent with the extent of the serpentinite stability field predicted for the convergence rates and ages of LAA subduction. Our data show a peak in boron isotopes, intraslab seismicity rates and volcanic production rates around Dominica, and this is where our forward models (Fig. 4b) predict a peak in dehydration from 0-2 Ma of subduction of the Marathon and Mercurius fracture zones. Therefore, our data indicate that enhanced fluid fluxing of the mantle wedge is associated with higher magma production in the LAA. However, because it is not possible to quantify the relative controls of flux melting versus decompression melting with the available data we cannot identify the cause of any relationship at present.

High ratios of small to large earthquakes (high *b*-values) on the plate interface and forearc[12] (Fig. 4c), as well as low shear-wave velocities (4.3 +/- 0.05 km/s) at 50 km depth (Fig. 4d, derived from Rayleigh waves recorded during the VoiLA seismic experiment[3] - see Methods) could reflect excess dehydration at shallower depths. High *b*-values are commonly attributed to seismogenic failure at lower stresses due to higher pore fluid pressures, while shear velocity anomalies of around 9% could correspond to about 1.1 vol. % of fluids and associated melts[32]. Shear velocities and *b*-values are characterised by a prominent maximum and minimum, respectively, in the region around Martinique, i.e. displaced southward from the peak in boron isotopes. Due to the obliquity of the fracture zones to the trench, excess forearc dehydration (derived from shallower slab depths) is expected to occur further to the south than dehydration below the arc, coincident with the *b*-value and shear velocity peaks (Fig. 4b).

Finally, there are systematic variations in crustal thickness along the arc[7], with thicknesses of around 35 km north of Martinique and around 30 km in the south. These reflect a long-term integrated variation in magma productivity. When we consider the excess dehydration over the age of the present arc (around 25 Myr), the position of Marathon-Mercurius fracture zone subduction has shifted from the north near St Kitts to Dominica today, hence a larger crustal thickness would be expected along the whole northern arc, as observed. Again, however, we cannot constrain the relative role of decompression melting in this magma production.

None of the other Atlantic fracture zones have contributed to dehydration below the arc. The 15-20 fracture zone has not subducted deep enough (but higher b-values and lower shear-wave velocities in the forearc near Antigua in Fig. 4 could, given spatial resolution of these measurements, indicate shallow fluid release from it). Other Atlantic fracture zones have yet to reach the trench. It is likely that there were fracture zones in the Proto-Caribbean oceanic lithosphere but their location is uncertain. We included in our model a single, large-offset fracture zone at the location required to fit the basin geometry between the Bahamas Bank and Demerara Rise (Fig. 1; see Methods). This yields a small peak in excess dehydration in the southernmost arc. Thus, within the uncertainties, Proto-Caribbean fracture zones could explain the increases in δ11B and *b*-values and decrease in shear velocities around St. Vincent and Grenada.

Given the geological complexity of subduction systems, our new geochemical and geophysical expressions of fluids along the LAA show remarkable coherence with the predicted history of fluid release from fracture zones in the subducting plate at different locations in the system and over different temporal windows. Furthermore, the high boron contents and elevated $\delta^{11}$B signature of melt inclusions in magmas from the central segment of the arc are unambiguous indicators of dehydration of subducted serpentine, which is expected to be one the main minerals formed in fracture zone hydration. Therefore, our observations provide strong evidence that a heterogeneous distribution of serpentine in subducting mantle lithosphere exerts a primary control on along-arc variations in mantle wedge hydration and seismicity and may also influence the crustal structure and magmatic productivity of volcanic arcs.

## References

1. Hacker, B. R. H2O subduction beyond arcs. *Geochem. Geophys. Geosystems* **9**, (2008).
2. Grevemeyer, I., Ranero, C. R. & Ivandic, M. Structure of oceanic crust and serpentinization at subduction trenches. *Geosphere* **14**, 395–418 (2018).
3. Goes, S. *et al.* Project VoiLA: Volatile Recycling in the Lesser Antilles. *Eos* **100**, (2019).
4. Wadge, G. Comparison of volcanic production rates and subduction rates in the Lesser Antilles and Central America. *Geology* **12**, 555–558 (1984).
5. Boynton, C. H., Westbrook, G. K., Bott, M. H. P. & Long, R. E. A seismic refraction investigation of crustal structure beneath the Lesser Antilles island arc. *Geophys. J. R. Astron. Soc.* **58**, 371–393 (1979).
6. Macdonald, R., Hawkesworth, C. J. & Heath, E. The Lesser Antilles volcanic chain: a study in arc magmatism. *Earth-Sci. Rev.* **49**, 1–76 (2000).
7. Melekhova, E. *et al.* Lateral variation in crustal structure along the Lesser Antilles arc from petrology of crustal xenoliths and seismic receiver functions. *Earth Planet. Sci. Lett.* **516**, 12–24 (2019).
8. Hayes, G. P., McNamara, D. E., Seidman, L. & Roger, J. Quantifying potential earthquake and tsunami hazard in the Lesser Antilles subduction zone of the Caribbean region. *Geophys. J. Int.* **196**, 510–521 (2014).
9. Keken, P. E. van, Hacker, B. R., Syracuse, E. M. & Abers, G. A. Subduction factory: 4. Depth-dependent flux of H2O from subducting slabs worldwide. *J. Geophys. Res. Solid Earth* **116**, (2011).

10. Carpentier, M., Chauvel, C. & Mattielli, N. Pb–Nd isotopic constraints on sedimentary input into the Lesser Antilles arc system. *Earth Planet. Sci. Lett.* **272**, 199–211 (2008).

11. Bouysse, P. & Westercamp, D. Subduction of Atlantic aseismic ridges and Late Cenozoic evolution of the Lesser Antilles island arc. *Tectonophysics* **175**, 349–380 (1990).

12. Schlaphorst, D. *et al.* Water, oceanic fracture zones and the lubrication of subducting plate boundaries—insights from seismicity. *Geophys. J. Int.* **204**, 1405–1420 (2016).

13. Müller, R. D. *et al.* A Global Plate Model Including Lithospheric Deformation Along Major Rifts and Orogens Since the Triassic. *Tectonics* **38**, 1884–1907 (2019).

14. Escartín, J. *et al.* Central role of detachment faults in accretion of slow-spreading oceanic lithosphere. *Nature* **455**, 790–794 (2008).

15. Manea, V. C., Leeman, W. P., Gerya, T., Manea, M. & Zhu, G. Subduction of fracture zones controls mantle melting and geochemical signature above slabs. *Nat. Commun.* **5**, 5095 (2014).

16. Bach, W. & Früh-Green, G. L. Alteration of the Oceanic Lithosphere and Implications for Seafloor Processes. *Elements* **6**, 173–178 (2010).

17. De Hoog, J. C. M. & Savov, I. P. Boron Isotopes as a Tracer of Subduction Zone Processes. in *Boron Isotopes: The Fifth Element* (eds. Marschall, H. & Foster, G.) 217–247 (Springer International Publishing, 2018). doi:10.1007/978-3-319-64666-4_9.

18. Leeman, W. P., Tonarini, S. & Turner, S. Boron isotope variations in Tonga-Kermadec-New Zealand arc lavas: Implications for the origin of subduction components and mantle influences. *Geochem. Geophys. Geosystems* **18**, 1126–1162 (2017).

19. Leeman, W. P. Boron and other fluid-mobile elements in volcanic arc lavas: Implications for subduction processes. *Wash. DC Am. Geophys. Union Geophys. Monogr. Ser.* **96**, 269–276 (1996).

20. Tonarini, S., Leeman, W. P. & Leat, P. T. Subduction erosion of forearc mantle wedge implicated in the genesis of the South Sandwich Island (SSI) arc: Evidence from boron isotope systematics. *Earth Planet. Sci. Lett.* **301**, 275–284 (2011).

21. Marschall, H. R. Boron Isotopes in the Ocean Floor Realm and the Mantle. in *Boron Isotopes: The Fifth Element* (eds. Marschall, H. & Foster, G.) 189–215 (Springer International Publishing, 2018). doi:10.1007/978-3-319-64666-4_8.

22. Bezard, R. *et al.* Assimilation of sediments embedded in the oceanic arc crust: myth or reality? *Earth Planet. Sci. Lett.* **395**, 51–60 (2014).

23. Plank, T. 4.17 - The Chemical Composition of Subducting Sediments. in *Treatise on Geochemistry (Second Edition)* (eds. Holland, H. D. & Turekian, K. K.) 607–629 (Elsevier, 2014). doi:10.1016/B978-0-08-095975-7.00319-3.

24. Benton, L. D., Ryan, J. G. & Tera, F. Boron isotope systematics of slab fluids as inferred from a serpentine seamount, Mariana forearc. *Earth Planet. Sci. Lett.* **187**, 273–282 (2001).

25. Kaliwoda, M. *et al.* Boron and boron isotope systematics in the peralkaline Ilímaussaq intrusion (South Greenland) and its granitic country rocks: A record of magmatic and hydrothermal processes. *Lithos* **125**, 51–64 (2011).

26. Jones, R. E. *et al.* Temporal variations in the influence of the subducting slab on Central Andean arc magmas: Evidence from boron isotope systematics. *Earth Planet. Sci. Lett.* **408**, 390–401 (2014).

27. McCaig, A. M. *et al.* No significant boron in the hydrated mantle of most subducting slabs. *Nat. Commun.* **9**, 1–10 (2018).

28. Paulatto, M. *et al.* Dehydration of subducting slow-spread oceanic lithosphere in the Lesser Antilles. *Nat. Commun.* **8**, 15980 (2017).

29. Vils, F., Tonarini, S., Kalt, A. & Seitz, H.-M. Boron, lithium and strontium isotopes as tracers of seawater–serpentinite interaction at Mid-Atlantic ridge, ODP Leg 209. *Earth Planet. Sci. Lett.* **286**, 414–425 (2009).

30. Bie, L. *et al.* Along□Arc Heterogeneity in Local Seismicity across the Lesser Antilles Subduction Zone from a Dense Ocean□Bottom Seismometer Network. *Seismol. Res. Lett.* **91**, 237–247 (2020).

31. Kirby, S., Engdahl, R. E. & Denlinger, R. Intermediate-Depth Intraslab Earthquakes and Arc Volcanism as Physical Expressions of Crustal and Uppermost Mantle Metamorphism in Subducting Slabs. in *Subduction* 195–214 (American Geophysical Union (AGU), 2013). doi:10.1029/GM096p0195.

32. Hammond, W. C. & Humphreys, E. D. Upper mantle seismic wave velocity: Effects of realistic partial melt geometries. *J. Geophys. Res. Solid Earth* **105**, 10975–10986 (2000).

33. Gurenko, A. A., Trumbull, R. B., Thomas, R. & Lindsay, J. M. A melt inclusion record of volatiles, trace elements and Li–B isotope variations in a single magma system from the Plat Pays Volcanic Complex, Dominica, Lesser Antilles. *J. Petrol.* **46**, 2495–2526 (2005).

34. Bouvier, A.-S., Métrich, N. & Deloule, E. Light elements, volatiles, and stable isotopes in basaltic melt inclusions from Grenada, Lesser Antilles: Inferences for magma genesis. *Geochem. Geophys. Geosystems* **11**, (2010).

35. Bouvier, A.-S., Manzini, M., Rose-Koga, E. F., Nichols, A. R. L. & Baumgartner, L. P. Tracing of Cl input into the sub-arc mantle through the combined analysis of B, O and Cl isotopes in melt inclusions. *Earth Planet. Sci. Lett.* **507**, 30–39 (2019).

## End notes

## Data availability statement

All geochemical data generated during this study are included in this published article (and its supplementary information files) and can be accessed in the EarthChem repository (https://doi.org/XXXX/XXXX). Compiled geochemical data is freely available from the GEOROC database. Metadata of the VoiLA broadband OBS network and used land stations, a catalogue of the local earthquakes, and teleseismic Rayleigh wave data can be accessed through the Zenodo repository: https://doi.org/10.5281/zenodo.3725528. All broadband OBS data collected by the VoiLA project will become freely available through the IRIS DMC (Data Management Center) via their data request tools, at the end of the project (April 2021).

## VOILA team consortium

George F. Cooper[1], Colin G. Macpherson[2], Jon D. Blundy[1], Benjamin Maunder[3], Robert W. Allen[3], Saskia Goes[3], Jenny Collier[3], Lidong Bie[5], Nick Harmon[4], Stephen P. Hicks[3], Andreas Rietbrock[5,6], Catherine Rychert[4], Jon P. Davidson[2], Richard G. Davy[3], Tim J. Henstock[4], Michael J. Kendall[2], David Schlaphorst[2], Jeroen van Hunen[2], Jamie J. Wilkinson[3,7], Marjorie Wilson[8]

[6] Geophysical Institute (GPI), Karlsruhe Institute of Technology, 76187 Karlsruhe, Germany

[7] Department of Earth Sciences, Natural History Museum, Cromwell Road, London SW7 5BD, UK

[8] School of Earth and Environment, University of Leeds, Leeds, LS2 9JT, UK

## Acknowledgements

We thank our project partners, Richard Robertson, Joan Latchman, Steve Tait and Frank Krüger for support and discussion over the course of this project. We thank C. J. de Hoog for assistance with SIMS analysis at the Edinburgh Ion Microprobe Facility and Stuart Kearns for help with EPMA analysis, the German Instrument Pool for Amphibian Seismology (DEPAS), hosted by the Alfred Wegener Institute Bremerhaven, for providing the ocean-bottom and temporary island seismometers, and UCSD (Scripps) for providing additional ocean-bottom seismometers. This research was funded by the VoiLA NERC consortium grant (NE/K010824/1). SIMS analysis was funded by EIMF proposals IMF619/0517 and IMF653/0518.

## Author Contributions

All authors discussed the results and implications of the work and commented on the manuscript at all stages. G.F.C., C.G.M., J.D.B., and A.A.I carried out geochemical analysis and interpretation. G.F.C, S.G., C.G.M, J.D.B., and J.C. drafted the manuscript. N.H. and C.R. produced the shear-wave velocity model. B.M. made the dehydration model. L.B. and S.P.H compiled local seismicity data, D.S. mapped b-values. R.W.A and J.C. produced the tectonic reconstruction and associated figures. C.G.M., S. G., J. D. B., J.C., A.R., N.H., C.R., J.P.D., T.J.H., J.v.H., J.J.W and M.W designed the original VoiLA experiment.

## Author Information Statement

Reprints and permissions information is available at www.nature.com/reprints.

The authors declare no competing interests.

Correspondence and requests for materials should be addressed to CooperG3@cardiff.ac.uk

## Figure Captions

**Fig. 1.** Bathymetric map of the study area showing the islands of the Lesser Antilles Arc (LAA, red). Map shows locations of the trench (purple line), oceanic fracture zones (black

lines, dashed where subducted), boundary between the proto-Caribbean and equatorial Atlantic seafloor (red line) and South American continent-ocean boundary (yellow line). Proto-Caribbean fracture zones have fully subducted; the likely location of a single one, required by basin geometry, is shown as a light dashed line. The bathymetric contrast between the northern and southern forearc is due to a strong difference in sediment thickness (from a few km in the north to > 15 km in the Barbados accretionary prism). Depth contours of the slab below the LAA are shown every 20 km (light blue lines) and every 100 km (dark blue lines). See Methods and Extended Data Figures 1 and 2 for further details.

**Fig. 2.** Bathymetric map of the Lesser Antilles Arc compared to water, B/Nb ratios, and $\delta^{11}B$ of melt inclusions in lavas. $H_2O$ (this study and compiled published values) and B/Nb symbols are coloured by the $SiO_2$ wt% of melt inclusions, as an indicator of magmatic differentiation. $\delta^{11}B$ symbols are coloured by B/Nb as an indicator of fluid addition. Previously published boron isotope ratios from melt inclusions[33–35] are shown as crosses. Error bars on $\delta^{11}B$ values represent propagated 1σ uncertainties and are typically <±1‰.

**Fig. 3.** Melt inclusion Nb/B versus $\delta^{11}B$ for Lesser Antilles Arc magmas from this study. Mixing model (black lines) shows contamination of depleted mantle (DM, grey square) by fluid derived from serpentinite and from altered oceanic crust (AOC) + sediment-derived fluids at 120 km depth. Green bar represents global serpentinite range. Red and green numbers represent the percentage by mass of fluid from the two sources added to the mantle. Inputs for the model are detailed in Methods. Dotted lines indicate composite fluids formed by mixing between (0.1% and 1% mass) fluids from the two discrete sources.  Shading indicates >60% (green), 30-60% (blue), and <30% (yellow) contribution from subducted serpentinite. Darker and lighter shaded areas represent domains referred to in text as ‘high’

and 'low' fluid contributions, respectively. Only samples measured in this study are plotted. Error bars on $\delta^{11}B$ values represent propagated 1σ uncertainties and are smaller than symbol size where absent. All 1σ uncertainties are typically <±1‰.

**Fig. 4.** Summary of along-arc geochemical and geophysical data. (a) Boron isotope ratios of melt inclusions with latitude in the LAA (data symbols coloured as in Fig. 3; previously published data[33–35] shown by crosses). Light and dark coloured shaded areas correspond to those in Fig. 3. (b) Modelled sub-arc excess (i.e. fracture-zone associated) dehydration averaged over the past 2 Myr (solid red line for fluids released below the arc, dashed yellow line below the forearc) and 25 Myr (dotted blue line, below the arc) (based on plate reconstruction and slab geometry, see Methods). (c) *b*-value distribution (relative frequency of small vs large events below the forearc)[12]. (d) Shear-wave velocity from teleseismic Rayleigh waves at 50 km depth, with main anomalies below the forearc. (e) Local seismicity in the subducting plate[30]. (f) Volcanic production rates over the last 100 kyr as dense-rock-equivalent volumes (DREV)[3] (red lines). (g) Crustal thickness below the arc from receiver functions[7] (blue line). Note how the modelled trends compare well with the main anomalies in data sensitive to recent fluid release below the fore-arc (c,d), below the arc (e,f) and over the past 25 Myr (g).

## Methods

### Geochemistry

#### a) Sample preparation

Crystals were separated from crushed and sieved scoria, pumice or lava. Picked crystals from the 0.5-1 mm and 1-2 mm size fractions were mounted on glass slides within 2.5 cm diameter aluminium rings, back-filled with epoxy resin, and polished to expose the centre of the crystals. Crystals were imaged under transmitted light to locate the most suitable glassy inclusions before further polishing to expose the maximum number of melt inclusions. All epoxy mounts were gold-coated prior to SIMS analysis.

### b) Trace elements by SIMS

We measured concentrations of $H_2O$, $CO_2$ and trace elements in 198 melt inclusions using the Cameca IMS-4f at the NERC Edinburgh Ion Micro-Probe Facility (EIMF), over two sessions (October 2017 and January 2018). The IMS-4f instrument was run with a 15 kV (nominal) primary beam of $O^-$ ions with a beam current of ~5 nA, resulting in a spot size at the sample surface of ~15 μm diameter. Positive secondary ions were extracted at 4.5 kV, using energy filtering with an energy window of 50±25 eV (for $CO_2$ analysis) or 75±25 eV (for all other elements). $CO_2$ measurements were performed first. Prior to each analysis, the sample was pre-sputtered using a primary beam raster of 20 μm for 4 minutes to reduce C backgrounds resulting from surface contamination. The isotopes $^{12}Mg^{2+}$, $^{12}C$, $^{26}Mg$, and $^{30}Si$ were measured. Peak positions were verified at the start of each analysis. The background C signal was determined through analysis of the nominally C-free KL2-G glass standard. Following $CO_2$ analysis, $H_2O$ and trace element concentrations were measured on the same analytical spot as the $CO_2$ analyses, using a secondary accelerating voltage of 4500 V with 75 V offset and a 25 μm image field. The isotopes $^{1}H$, $^{7}Li$, $^{11}B$, $^{19}F$, $^{26}Mg$, $^{35}Cl$, $^{30}Si$, $^{42}Ca$, $^{44}Ca$, $^{45}Sc$, $^{47}Ti$, $^{84}Sr$, $^{85}Rb$, $^{88}Sr$, $^{89}Y$, $^{90}Zr$, $^{93}Nb$, $^{133}Cs$, $^{138}Ba$, $^{139}La$, $^{140}Ce$, and $^{149}Sm$ were measured. Calibration was carried out on a range of basaltic glass standards with 0–4 wt.% $H_2O$, repeated throughout the day. Absolute element concentrations were calculated using the inhouse JCION5 software and by normalizing the intensities to Si (as measured using $^{30}Si$) which was determined by subsequent electron microprobe analysis. A summary of repeat analyses of GSD-1G and T1-G are presented in the Supplementary Data.

### c) Electron microprobe

Following volatile and trace element analysis, we measured major elements using a Cameca SX100 electron microprobe (EPMA) at the University of Bristol, UK. The gold coat was removed and samples were carbon-coated. Concentrations of $SiO_2$, $TiO_2$, $Al_2O_3$, $Fe_2O_3$, MnO, MgO, CaO, $Na_2O$, $K_2O$, $P_2O_5$, $Cr_2O_3$, $SO_2$, and Cl in glass were made with a 20 kV accelerating voltage, a 4 nA beam current and a 5 µm or 10 µm defocused beam to minimise alkali loss[36]. Major elements were calibrated using a range of synthetic oxide, mineral and metal standards.

### d) Boron isotopes by SIMS

Prior to boron isotope analysis, crystals hosting the measured melt inclusions were cut out of the epoxy mounts and pressed into indium within 24 mm diameter Al holders. This step reduced the total number of sample mounts and, as indium outgasses less than epoxy, reduces the time required to reach a suitable vacuum for analysis.

We measured boron isotopes ($^{11}B$ and $^{10}B$) in 92 melt inclusions using the Cameca IMS-1270 at the NERC Edinburgh Ion Micro-Probe Facility (EIMF), in December 2018. Prior to analysis, the samples were cleaned and a gold coat was applied. Positive secondary ions of $^{10}B^+$ and $^{11}B^+$ were produced by sputtering the sample with a 5nA, $^{16}O^{2-}$ primary beam with a net impact energy of 22 keV, focused using Köhler illumination to a ~25µm spot size. Secondary ions were extracted at 10 kV and counted by a single electron multiplier detector.

No energy filtering was applied. Analyses were performed using a mass resolution (M/ΔM) of ~2400. Single analyses consisted of 50 measurement cycles of $^{10}B$ and $^{11}B$ signals, using counting times of 2 s. Instrumental fractionation was determined using the reference materials GSD1-G, B6, GOR132-G, StHs6/80-G and BCR2-G, measured at the beginning, during and end of the session (Supplementary Data).

**Boron mixing model**

Element contents for AOC and sediment and serpentinite-derived fluids are from ref.[20]. Isotope ratios used for serpentinite fluids lie within the range of Atlantic peridotites[29,37–39] . Depleted Mantle boron concentrations and isotope ratios are from ref.[40]; Nb concentrations are from ref.[41]. Values are presented in Extended Data Table 1. Composite fluids are produced by mixing the two most significant endmembers in the Lesser Antilles (AOC + sediment and serpentinite derived fluid).

**Shear velocity**

The ocean-bottom seismic data analysed in this study were collected during two cruises aboard the RRS James Cook[42,43]. We used vertical seismograms to measure the amplitude and phase of ambient noise cross correlation function and teleseismic Rayleigh Waves. The onshore and offshore data were corrected for instrument response, detrended and demeaned prior to processing. The teleseismic data were further processed as detailed in ref.[9]. Measurements of Rayleigh wave dispersion and estimates of the amplitude at selected period were made using frequency-time analysis[44,45]. We measured dispersion from 18-11 s period. We used up to 2486 dispersion measurements from 93 events from teleseismic Rayleigh waves in the tomography.

Shear velocity tomography was performed in two steps: first the amplitude and phase data were inverted for phase velocity maps[46–48] and then at each location in the phase velocity maps we inverted for 1D shear velocity structure to generate a 3-D volume[46]. For the shear velocity inversion, we included the effects of the water column and sediment using *a priori* information; our initial crustal thickness was based on Airy isostasy across the region. The shear velocity inversion subsequently solved for the best fitting crustal thickness as well as shear velocity.

## Plate reconstruction and hydration modelling

### a) Mapping the tectonic features

Our modelling of the subducted features below the Lesser Antilles is based upon the global plate reconstruction of ref.[13] as implemented within the software G-Plates 2.1. In this reconstruction, the opening of the proto-Caribbean seaway occurs from 150 Ma through symmetrical seafloor spreading between the diverging North American and South America/African plates. For ease of reference, we will refer to this stage as the "proto-Caribbean and central Atlantic" opening. Breakup between the South American and African plates starts around 100 Ma with northward propagation from the south Atlantic. We refer to this second stage of seafloor spreading as "equatorial Atlantic" opening.

Most of the proto-Caribbean oceanic lithosphere has been subducted, but there remains a small segment in the south of the study area. The rifted oceanic lithosphere boundary between it and the equatorial Atlantic is visible in satellite gravity to the north-west of the Demerara Rise where it clearly acts as the termination point for a number of small fracture zones south of Doldrums Fracture Zone (red ellipse, Extended Data Fig  1b).

We first compared major Atlantic fracture zones in the region (15-20, Marathon, Mercurius, Vema and Doldrums) as detected in satellite gravity data to modelled flow lines according to the Müller et al. (2019) model (Extended Data Fig 1). Overall, the largest misfit between the two was ~50 km, and we assign this value to the positional uncertainty of these features (see below). The geometrical relationships between the two phases of seafloor spreading are particularly clear on the African side of the Atlantic, where the sediment cover is thin and the full sequence preserved (compared to the sedimented and partially subducted American side). The analysis showed that the southern two fracture zones (Vema and Doldrums) have only just reached the Lesser Antilles trench, whereas the northern fracture zone (15-20) only grazes the Lesser Antilles subduction zone.  None of these three fracture zones are therefore sources of hydration below the Lesser Antilles Arc.

Next we refined the location of the proto-Caribbean / equatorial Atlantic Ocean boundary through time (Extended Data Fig.2) based upon two observations. 1) The oldest section of the Marathon and Mercurius fracture zones can be well fitted by a flowline based entirely upon relative motion between North America and Africa. Therefore, this region must have lain entirely north of (or upon) the boundary between the central Atlantic and proto-Caribbean prior to opening of the equatorial Atlantic. 2) The major fracture zones to the south (Vema and Doldrums) can be well fitted by a flowline based entirely upon relative motion between South America and Africa.  In this case, the far western extent of these fracture zones (which is constrained by symmetry with the clearly observable extent of fracture zones on the African side) must mark the edge of the proto-Caribbean oceanic crust in order for the Demerara Rise to close back against the African continental margin prior to initiation of equatorial Atlantic spreading (Extended Data Fig 2a). Finally, the proto-Caribbean spreading ridge was placed mid-way between the separating North and South America plates, with a minimum number of transform faults inserted to satisfy the continental plate geometries. Using this updated geometry for the proto-Caribbean / equatorial Atlantic boundary, and our computed flowlines for the Marathon, Mercurius and unnamed proto-Caribbean fracture zones, we model the subduction of these incoming plate features beneath the Caribbean plate from 50 Ma through to the present day. Convergence azimuths and velocities between the Caribbean plate and the Atlantic are extracted directly from the model of ref.[13].

### b) Projecting tectonic features onto the slab

To properly track the features once they enter the subduction zone and the slab begins to dip, it is necessary to adjust their horizontal velocities. To do this, we use three different assumptions for how the slab deforms as it enters the subduction zone. One end-member is the "kinematic" approach outlined in ref.[49] whereby features are assumed to follow streamlines over the surface of a slab with a fixed geometry, i.e. minimal to no plate stretching during subduction. We use the slab geometry of ref.[30] determined using local seismicity, and ref.[50], which is based on teleseismic tomography, for the regions that this first model does not cover. We also assume that the slab geometry remains fixed relative to the Caribbean plate for the modelled time period. In the other end-member, the slab is assumed to maintain its horizontal velocity and acquire an additional vertical sinking velocity, which would imply some amount of plate stretching. For the plate motions of the region, the first approach places incoming plate features further south than the second. We run a third, "best-estimate" model that is intermediate between the two.

### c) Dehydration modelling

As incoming plate features move into the subduction zone, they dehydrate. Major pulses of subducting-plate dehydration occur[9] below the forearc and at subarc depths. Forearc dehydration includes the expulsion of pore fluids and the first breakdown of hydrous phases in the oceanic crust, while the subarc pulse starts with the blueshist transition that initiates directly below the maximum decoupling depth, below which the cool subducting plate first becomes coupled to the hot convecting mantle wedge. Following ref.[1] in computing phase stability fields, and using the kinematic thermal model set up of ref.[51] to compute a thermal structure for the geometry and velocity of the Antilles slab, we predict that the first pulse of dehydration extends down to about 40 km depth, and the subarc pulse peaks at a depth up to 100-120 km (based on preliminary tomographic models by ref.[52]). In a similar model for the Greek subduction zone (which is similarly slow and old as the Antilles), the main dehydration depth intervals agree with regions of high Vp/Vs above the slab, as expected from fluid release[53]. Motivated by these thermal models, sub-arc observations (number of Benioff zone earthquakes) and observations at the volcanic arc itself (boron isotopic signature, present day volcanic output and crustal thickness) are compared at a dehydration depth of 100 km, which matches the average sub-arc slab depth. Comparisons with observations that reflect conditions beneath the fore-arc (forearc Vs and b-value anomalies), are done at a dehydration depth of 40 km.

For this study, our interest is in lateral variations in water input. We assume that the fracture zones and Atlantic-Proto-Caribbean boundary are all sources of excess slab hydration, i.e. where the slab incorporates significantly larger quantities of water, mainly in the form of serpentinite, than in the plate away from the fracture zones., based on observations of similar structures offshore central America[54]. In the modelling, we apply the same Gaussian excess hydration profile with a width of 15 km to all these features (i.e. in addition to the uniform background). This width is informed by the lateral extent of the Vp/Vs anomaly observed underneath the Marathon fracture zone on the incoming plate[56]. To put a very approximate, order-of-magnitude estimate on the absolute values for the rate of excess hydration along the arc due to the subduction of each feature, we assume that the region of anomalous Vp/Vs corresponds to 50% serpentinised mantle lithosphere, and that half of this additional water is released under the fore-arc and half under the arc. We only model the along strike-variations in excess dehydration (i.e. we set background hydration to zero).

We ultimately use the models to calculate the relative rate of hydration along the arc over the past 2 Myr for meaningful comparison with features that should depend on the present day/recent dehydration below the arc and fore-arc, and over the past 25 Myr (the age of the current arc) for meaningful comparison with features that should depend on the total amount of water supplied to the arc (i.e. the crustal thickness). The results of these calculations are presented in Extended Data Fig. 4 for a "best estimate" calculation which uses the "halfway" approach to slab deformation; a "southern bound" calculation, which uses the stretched-slab end member plus a 50 km shift to the south (the maximum misfit between our modelled fracture zones and the actual fracture zones on the African side of the Atlantic); and a "northern bound" model which uses the "minimal-stretching" approach[49] plus a 50 km shift to the north.

### d) Key results

If we take the best estimate model, we predict that the dehydration peak due to the Marathon and Mercurius fracture zones and the Proto-Caribbean / equatorial Atlantic plate boundary lies currently underneath Dominica (solid red line). In the main article, we demonstrate that this corresponds well with the peak in $\delta^{11}$B, sub-arc Wadati-Benioff earthquakes and volcanic output. We also predict that, if these three features are dehydrating underneath the fore-arc, then they would currently be doing so trenchwards of Martinique (dashed yellow line). This corresponds well with anomalies in Vs at a depth of around 50 km and the *b*-values for earthquakes in the fore-arc/plate-interface region. Looking at the full history of the arc (0-25 Ma: dotted blue line), there is a broad peak between Dominica and St. Kitts and Nevis; the northern part of the arc. This higher rate of fluid flux in the north of the arc throughout the lifetime of the current arc may have resulted in a higher long-term magmatic output and therefore, a thicker crust[7] if flux melting occurred. However, we cannot constrain the relative contribution of flux melting versus decompression melting. There are also peaks in the present-day dehydration rate and long-term dehydration rate in the far south of the arc between Grenada and St. Vincent. These are due to the subduction of the unnamed proto-Caribbean fracture zone, the exact position of which is more speculative than for the Atlantic features. However, such features on the proto-Caribbean plate could potentially be responsible for the $\delta^{11}B$ anomaly observed at St. Vincent.

## References for methods

36. Humphreys, M. C. S., Kearns, S. L. & Blundy, J. D. SIMS investigation of electron-beam damage to hydrous, rhyolitic glasses: Implications for melt inclusion analysis. *Am. Mineral.* **91**, 667–679 (2006).
37. Boschi, C. *et al.* Serpentinization of mantle peridotites along an uplifted lithospheric section, Mid Atlantic Ridge at 11° N. *Lithos* **178**, 3–23 (2013).
38. Boschi, C., Dini, A., Früh-Green, G. L. & Kelley, D. S. Isotopic and element exchange during serpentinization and metasomatism at the Atlantis Massif (MAR 30°N): Insights from B and Sr isotope data. *Geochim. Cosmochim. Acta* **72**, 1801–1823 (2008).

39. Spivack, A. J. & Edmond, J. M. Boron isotope exchange between seawater and the oceanic crust. *Geochim. Cosmochim. Acta* **51**, 1033–1043 (1987).

40. Marschall, H. R. *et al.* The boron and lithium isotopic composition of mid-ocean ridge basalts and the mantle. *Geochim. Cosmochim. Acta* **207**, 102–138 (2017).

41. Workman, R. K. & Hart, S. R. Major and trace element composition of the depleted MORB mantle (DMM). *Earth Planet. Sci. Lett.* **231**, 53–72 (2005).

42. Collier, J. S. *VOILA - Volatile recycling in the Lesser Antilles arc: RRS James Cook cruise report JC133*. 79 https://www.bodc.ac.uk/resources/inventories/cruise_inventory/reports/jc133.pdf (2015).

43. Collier, J. S. *VOILA - Volatile recycling in the Lesser Antilles arc: RRS James Cook cruise report JC149*. 161 https://www.bodc.ac.uk/resources/inventories/cruise_inventory/reports/jc149.pdf (2017).

44. Landisman, M., Dziewonski, A. & Satô, Y. Recent Improvements in the Analysis of Surface Wave Observations. *Geophys. J. Int.* **17**, 369–403 (1969).

45. Levshin, A. L. & Ritzwoller, M. H. Automated Detection, Extraction, and Measurement of Regional Surface Waves. in *Monitoring the Comprehensive Nuclear-Test-Ban Treaty: Surface Waves* (eds. Levshin, A. L. & Ritzwoller, M. H.) 1531–1545 (Birkhäuser Basel, 2001). doi:10.1007/978-3-0348-8264-4_11.

46. Harmon, N. & Rychert, C. A. Joint inversion of teleseismic and ambient noise Rayleigh waves for phase velocity maps, an application to Iceland: Noise-Teleseismic Phase Velocity Maps. *J. Geophys. Res. Solid Earth* **121**, 5966–5987 (2016).

47. Forsyth, D. W. & Li, A. Array analysis of two-dimensional variations in surface wave phase velocity and azimuthal anisotropy in the presence of multipathing interference. *Seism. Earth Array Anal. Broadband Seism.* **157**, 81–97 (2005).

48. Yang, Y. & Forsyth, D. W. Regional tomographic inversion of the amplitude and phase of Rayleigh waves with 2-D sensitivity kernels. *Geophys. J. Int.* **166**, 1148–1160 (2006).

49. Harmon, N. *et al.* Mapping geologic features onto subducted slabs. *Geophys. J. Int.* **219**, 725–733 (2019).

50. Brazuz, B. 3D teleseismic travel time tomography along the Lesser Antilles subduction zone. (Karlsruhe Institute of Technology, Faculty of Physics, Geophysical Institute, 2019).

51. Perrin, A. *et al.* Reconciling mantle wedge thermal structure with arc lava thermobarometric determinations in oceanic subduction zones. *Geochem. Geophys. Geosystems* **17**, 4105–4127 (2016).

52. Hicks, S. P. *et al.* Evidence for an Anomalously Large Cold Mantle Wedge Corner of the Caribbean Plate in the Lesser Antilles Subduction Zone. in *AGU Fall Meeting 2019* (AGU, 2019).

53. Halpaap, F. *et al.* Earthquakes track subduction fluids from slab source to mantle wedge sink. *Sci. Adv.* **5**, eaav7369 (2019).

54. Avendonk, H. J. A. V., Holbrook, W. S., Lizarralde, D. & Denyer, P. Structure and serpentinization of the subducting Cocos plate offshore Nicaragua and Costa Rica. *Geochem. Geophys. Geosystems* **12**, (2011).

55. Sandwell, D. T., Müller, R. D., Smith, W. H. F., Garcia, E. & Francis, R. New global marine gravity model from CryoSat-2 and Jason-1 reveals buried tectonic structure. *Science* **346**, 65–67 (2014).

## Extended Data

**Extended Data Fig. 1.** a) Modelled fracture zones in the central Atlantic, overlain on an oceanic crust age grid from ref.[13]. Coloured stars denote conjugate points associated with opening of the equatorial Atlantic at either end of the Vema (green) and Doldrums (yellow) fracture zones and between the Demerara rise and African continental margin (red). b) Modelled fracture zones overlain on satellite free-air gravity[55]. Red ellipse marks the location of the proto-Caribbean / Atlantic boundary.

**Extended Data Fig. 2.** Snap shot of modified plate reconstruction at 50Ma[13]. Velocity vectors (coloured by plate) shown are relative to the mantle reference frame. The figure shows the four sources of dehydration from the subducted slab over the past 25 Ma considered here ((i) Marathon FZ; (ii) Mercurius FZ; (iii) proto-Caribbean/ equatorial Atlantic boundary and (iv) unnamed FZ formed during proto-Caribbean opening – labelled PCFracture Zone)

**Extended Data Fig. 3.** All melt inclusion $\delta^{11}$B values measured in this study versus indicators of fluid composition (a, b), and differentiation (c-e). No clear observable trends are shown between islands, indicating that these differences are largely controlled by the mantle source.

**Extended Data Fig. 4.** The average rate of excess-dehydration (above a uniform background), resulting from the subduction of fracture zones and the proto-Caribbean / Atlantic plate boundary, along the arc from 11° N to 18° N over the past 2 Myr (red solid curve) and 25 Myr (blue dotted curve), and below the fore-arc over the past 2 Myr (dashed yellow line). The pattern of relative distribution of dehydration is robust, constrained by the history of fracture-zone/plate-boundary subduction, but the absolute values of the dehydration rates should be treated with caution, as they depend strongly on the simple model assumptions of the level of hydration and relative strength of fore- and sub-arc dehydration. Panel (a) is the best estimate (b) is the “northern bound” end-member and (c) is the “southern bound” (see text for details).

**Extended Data Table 1.** $\delta^{11}$B values, B concentrations, and Nb/B of sources of fluids used in the mixing model (Fig. 3).

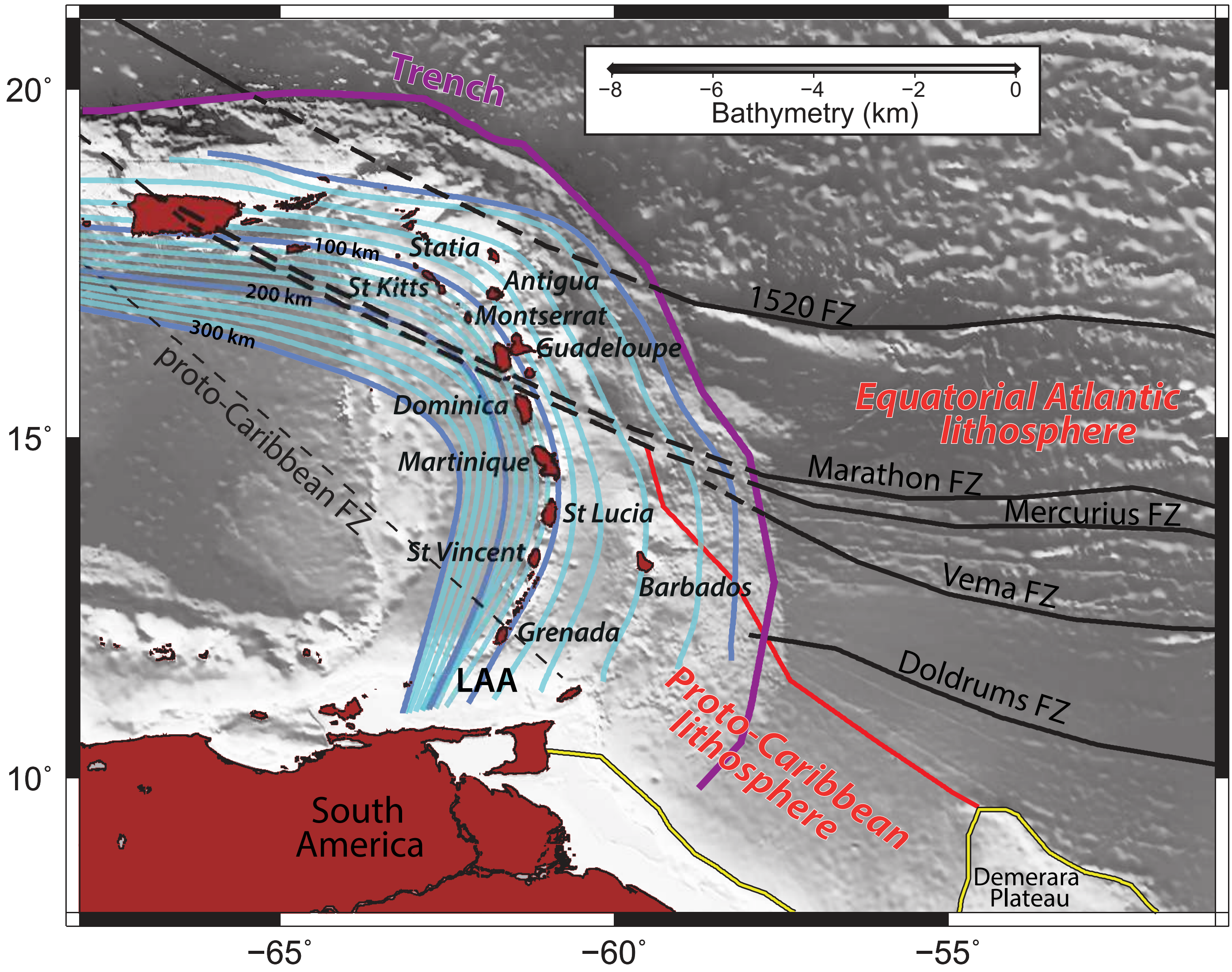
Trench
−8
−6
−4
−2
0
Bathymetry (km)
100 km
200 km
300 km
Statia
St Kitts
Antigua
Montserrat
Guadeloupe
Dominica
Martinique
St Lucia
St Vincent
Grenada
Barbados
LAA
1520 FZ
Equatorial Atlantic lithosphere
Marathon FZ
Mercurius FZ
Vema FZ
Doldrums FZ
proto-Caribbean FZ
Proto-Caribbean lithosphere
South America
Demerara Plateau
20°
15°
10°
−65°
−60°
−55°

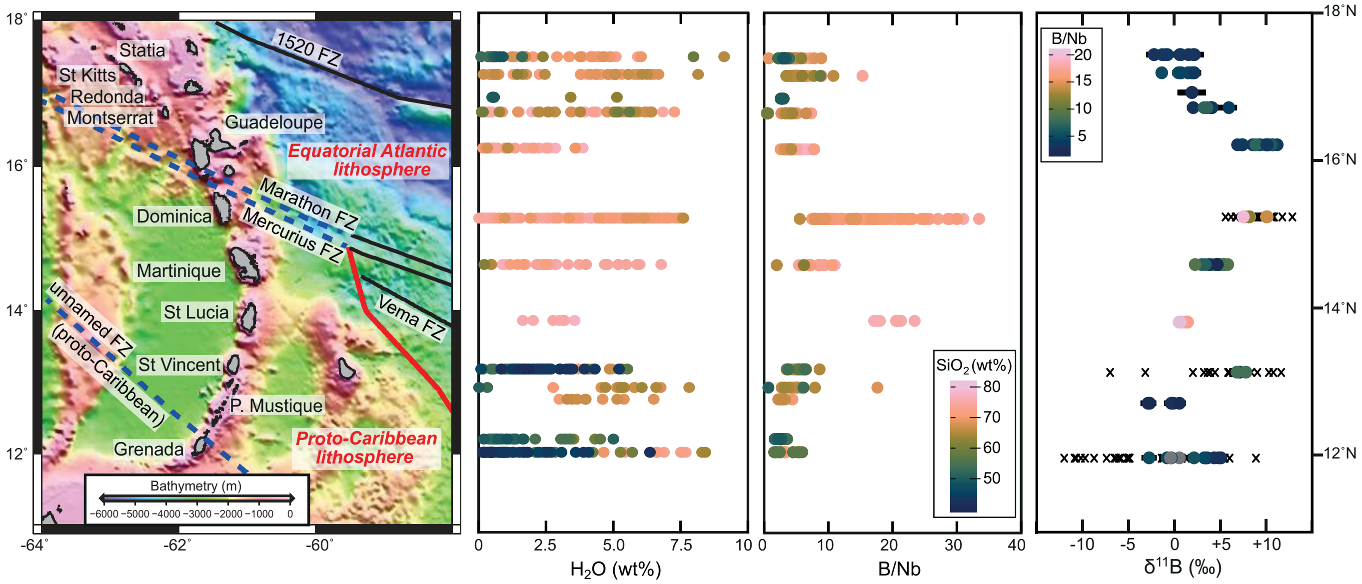
18°
16°
14°
12°
-64°
-62°
-60°
Statia
St Kitts
Redonda
Montserrat
Guadeloupe
1520 FZ
Equatorial Atlantic lithosphere
Marathon FZ
Mercurius FZ
Dominica
Martinique
St Lucia
Vema FZ
unnamed FZ (proto-Caribbean)
St Vincent
P. Mustique
Grenada
Proto-Caribbean lithosphere
Bathymetry (m)
−6000 −5000 −4000 −3000 −2000 −1000 0
0
2.5
5.0
7.5
10
$H_2O$ (wt%)
0
10
20
30
40
B/Nb
$SiO_2$ (wt%)
80
70
60
50
B/Nb
20
15
10
5
-10
-5
0
+5
+10
$\delta^{11}B$ (‰)
18°N
16°N
14°N
12°N

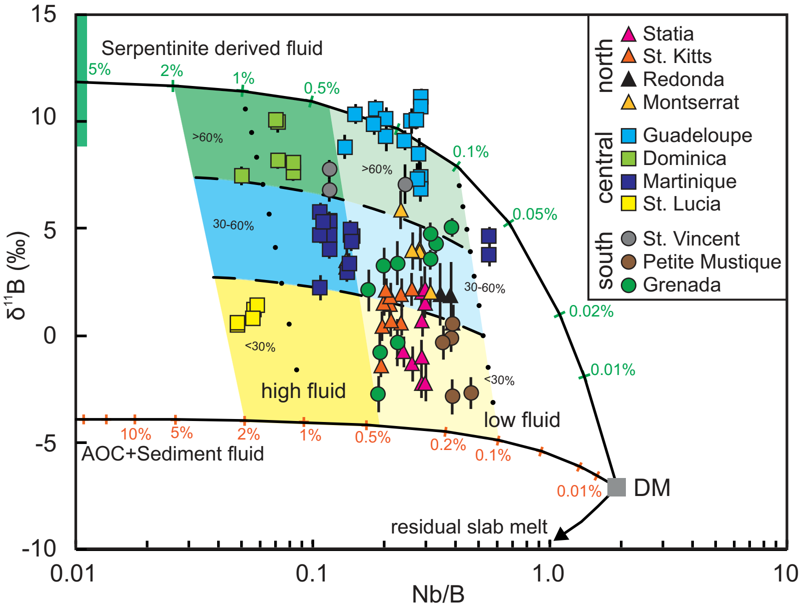

Serpentinite derived fluid
5%
2%
1%
0.5%
0.1%
0.05%
0.02%
0.01%
>60%
>60%
30-60%
30-60%
<30%
<30%
high fluid
low fluid
AOC+Sediment fluid
10%
5%
2%
1%
0.5%
0.2%
0.1%
0.01%
DM
residual slab melt
north
▲ Statia
▲ St. Kitts
▲ Redonda
▲ Montserrat
central
■ Guadeloupe
■ Dominica
■ Martinique
■ St. Lucia
south
● St. Vincent
● Petite Mustique
● Grenada
15
10
5
0
-5
-10
$\delta^{11}B$ (‰)
0.01
0.1
1.0
10
Nb/B

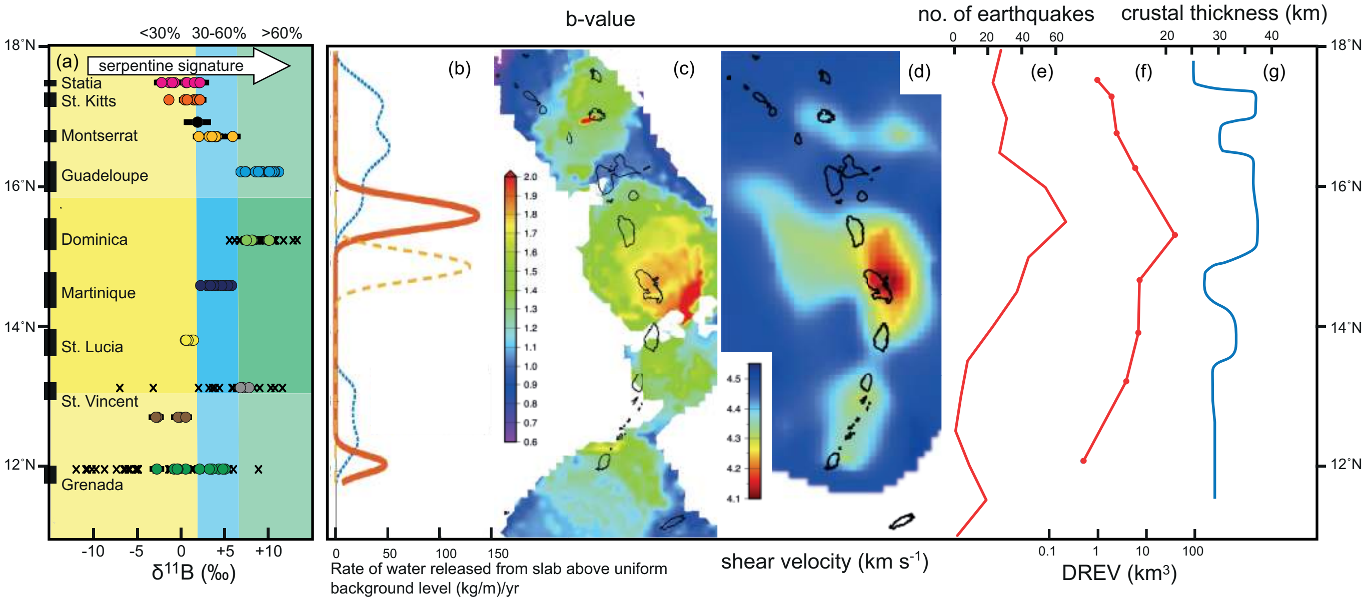
18°N
16°N
14°N
12°N
<30%
30-60%
>60%
(a)
serpentine signature
Statia
St. Kitts
Montserrat
Guadeloupe
Dominica
Martinique
St. Lucia
St. Vincent
Grenada
-10
-5
0
+5
+10
δ11B (‰)
b-value
(b)
(c)
2.0
1.9
1.8
1.7
1.6
1.5
1.4
1.3
1.2
1.1
1.0
0.9
0.8
0.7
0.6
0
50
100
150
Rate of water released from slab above uniform background level (kg/m)/yr
(d)
4.5
4.4
4.3
4.2
4.1
shear velocity (km s-1)
no. of earthquakes
0
20
40
60
(e)
crustal thickness (km)
20
30
40
(f)
(g)
0.1
1
10
100
DREV (km3)
18°N
16°N
14°N
12°N